



The “Blazar Sequence” in the TeV Band

Zhihao Ouyang¹, Hubing Xiao¹ , Jianzhen Chen¹, Junhui Fan^{3,4,5} , Anton A. Strigachev², Rumen S. Bachev² ,

Xiangtao Zeng^{3,4,5} , Marina Manganaro⁶, Rui Xue⁷ , and Zelin Li⁸

¹ Shanghai Key Lab for Astrophysics, Shanghai Normal University, Shanghai, 200234, People’s Republic of China; hubing.xiao@shnu.edu.cn, jzchen@shnu.edu.cn

² Institute of Astronomy and National Astronomical Observatory, Bulgarian Academy of Sciences, 72 Tsarigradsko shosse Blvd., 1784 Sofia, Bulgaria

³ Center for Astrophysics, Guangzhou University, Guangzhou, 510006, People’s Republic of China; fjh@gzhu.edu.cn

⁴ Key Laboratory for Astronomical Observation and Technology of Guangzhou, Guangzhou, 510006, People’s Republic of China

⁵ Astronomy Science and Technology Research Laboratory of Department of Education of Guangdong Province, Guangzhou, 510006, People’s Republic of China

⁶ Department of Physics, University of Rijeka, Rijeka, 51000, Croatia

⁷ Department of Physics, Zhejiang Normal University, Jinhua, 321004, People’s Republic of China

⁸ College of Microelectronics, Feicuihu Campus of Hefei University of Technology, Hefei, 230601, People’s Republic of China

Received 2022 December 27; revised 2023 March 8; accepted 2023 March 8; published 2023 May 26

Abstract

The “blazar sequence” has been proposed for more than 20 yr, yet its nature is still unclear. In this work, for the first time we expand this topic to the TeV band by using a sample of 58 TeV blazars, including 48 blazars in the quiescent state and 21 blazars in the flaring state (11 blazars show in both quiescent and flaring state). We investigate the correlation between the TeV luminosity, which has been compensated for attenuation from extragalactic background light, and the synchrotron peak frequency. We note that there is no correlation between TeV luminosity and peak frequency in the quiescent state and a strong anticorrelation in the flaring state for the observed value. However, there is a strong positive correlation in both the quiescent state and the flaring state for the intrinsic value. This indicates that the blazar sequence is shown in the flaring state rather than in the quiescent state for the observed value and the blazar sequence is not present in both states after removing the beaming effect. In addition, to confirm whether the beaming effect results in the blazar sequence, we compare the Fermi γ -ray luminosity between the quiescent state and the flaring state. We find the Fermi γ -ray luminosity in the flaring state is greater than that in the quiescent state, and the Doppler factor in the flaring state is greater. We suggest the blazar sequence in the flaring state may be due to a stronger beaming effect.

Unified Astronomy Thesaurus concepts: BL Lacertae objects (158); Flat-spectrum radio quasars (2163)

1. Introduction

Blazars are a subclass of active galactic nuclei (AGNs) with extreme observational properties, including high polarization, fast rapid variability, and strong high-energy γ -ray radiation, etc. (Urry & Padovani 1995; Fan et al. 2004, 2014a, 2016; Lyutikov & Kravchenko 2017; Ouyang et al. 2021; Xiao et al. 2022, and references therein). They are divided into two subclasses, flat-spectrum radio quasars (FSRQs) and BL Lacertae objects (BL Lacs), based on their optical spectrum. FSRQs have strong broad emission lines (rest-frame equivalent width, $EW \geq 5 \text{ \AA}$), while BL Lacs have weak or no emission lines ($EW < 5 \text{ \AA}$; Stickel et al. 1991; Urry & Padovani 1995; Scarpa & Falomo 1997). The blazar spectral energy distribution (SED) is characterized by a two-hump structure. The low-energy hump occurs at infrared to X-ray wavelengths, explained by the synchrotron emission from electrons. The high-energy hump occurs at MeV to GeV energies, which is produced either by the inverse Compton process in a leptonic scenario (Tavecchio et al. 1998; Ghisellini & Tavecchio 2009; Tan et al. 2020) or proton synchrotron emission in a hadronic scenario (Mücke et al. 2003; Böttcher et al. 2009; Cerruti et al. 2015; Cerruti et al. 2019), or even a hybrid scenario (Gao et al. 2019; Xue et al. 2022). According to the synchrotron peak frequency, blazars can be divided into low-synchrotron-peaked sources (LSPs), intermediate-synchrotron-peaked sources

(ISPs), and high-synchrotron-peaked sources (HSPs; Abdo et al. 2010; Fan et al. 2016; Yang et al. 2022a).

An increasing number of extragalactic sources are being detected in the TeV band, which is also known as the very-high-energy band (VHE; $E \gtrsim 100 \text{ GeV}$). Radiation in the VHE band is mainly detected by ground-based Cherenkov telescopes, e.g., the Major Atmospheric Gamma-ray Imaging Cherenkov Telescopes (MAGIC), the High Energy Stereoscopic System (H.E.S.S.), the Collaboration between Australia and Nippon for a Gamma Ray Observatory in the Outback, the Very Energetic Radiation Imaging Telescope Array System (VERITAS), and the Large High Altitude Air Shower Observatory. There are 251 TeV sources collected in TeVCat,⁹ and the number is gradually increasing. The number of TeV blazars is still small compared to GeV ones, but a lot of issues have been studied concerning these TeV blazars. Massaro et al. (2013) suggested criteria to select TeV BL Lac candidates based on infrared and X-ray observations; Lin & Fan (2016) compared the observational properties of TeV-detected BL Lacs with non-TeV-detected BL Lacs; Paiano et al. (2017) compiled 22 BL Lacs detected in TeV energy range and determined or constrained their redshifts, etc. Observations of TeV blazars are usually performed during their flaring state, while some are observed in their low-energy state (i.e., quiescent state) owing to certain circumstances, e.g., the source is bright enough even in a quiescent state. However, observations of TeV blazars in VHE γ -rays are not easy because of the strong absorption by the extragalactic



Original content from this work may be used under the terms of the [Creative Commons Attribution 4.0 licence](https://creativecommons.org/licenses/by/4.0/). Any further distribution of this work must maintain attribution to the author(s) and the title of the work, journal citation and DOI.

⁹ <http://tevcat2.uchicago.edu/>

background light (EBL; Franceschini et al. 2008; Domínguez et al. 2011): the absorption would steepen the TeV spectrum significantly.

Fossati et al. (1998) proposed a “blazar sequence,” from FSRQs to radio-selected BL Lacs and to X-ray-selected BL Lacs, whose synchrotron peak luminosity decreases with synchrotron peak frequency increase, which has been explained as a consequence of the difference of electron cooling efficiency (Ghisellini et al. 1998). The original blazar sequence was built with a few sources; Ghisellini et al. (2017) used the 3rd Catalog of AGN Detected by the Fermi-LAT sample and compiled all the archival data to build their average SED, which agrees with the original blazar sequence and verifies the existence of the blazar sequence. Many authors have performed many studies on this issue, and there exist basically two elucidations among these scholars. One acknowledges the validity of the blazar sequence, but differ from the original explanation. For instance, some studies have suggested it to be caused by the beaming effect (Nieppola et al. 2008; Fan et al. 2017; Yang et al. 2022b) and the different locations of the dissipation region for BL Lacs and FSRQs (Potter & Cotter 2015). The other interpretation argues that the blazar sequence is caused by observational biases (Giommi et al. 2012a, 2012b).

Study of the blazar sequence is still open. Whilst many of the previous works were carried out using monochromatic luminosity (radio, optical, X-ray, γ -ray, synchrotron peak luminosity) to study the blazar sequence, blazar studies in the TeV band have not yet been performed. Using TeV γ -ray data to investigate the blazar sequence is of great significance to understand the physical interpretation of the blazar sequence in the VHE band. In this work, for the purpose of exploring the blazar sequence in the TeV energy range, we will investigate the correlation between the TeV luminosity and the synchrotron peak frequency for TeV blazars.

The sample acquisition and quantity calculations are presented in Section 2. The results are given in Sections 3 and 4. The discussions and conclusions are given in Sections 5 and 6. In this work, we use the following flat Lambda cold dark matter cosmology, with $H_0 = 71 \text{ km s}^{-1} \text{ Mpc}^{-1}$, $\Omega_M = 0.27$, and $\Omega_\Lambda = 0.73$.

2. Sample

There are 81 blazars, of which 67 are BL Lacs, nine are FSRQs, and five are blazar candidates of uncertain type (BCUs), confirmed as TeV emitters by associating TeVCat and 4FGL_DR3 (Abdollahi et al. 2022). We collect the TeV spectrum information from the literature and the synchrotron peak frequency ($\log \nu_p^{\text{ob}}$) from Fan et al. (2016) and Yang et al. (2022a) for these sources. In this case, we compile a sample of 57 out of these 81 TeV blazars with available quiescent state or (and) flaring state TeV spectra. The quiescent state refers to a low flux density or being quiet and inactive or otherwise being an average flux density state, while the flaring state designates conspicuous transient brightening and shows an outburst in the TeV band. Moreover, we also include one source, 4FGL J2042.1+2427 (RGB J2042.1+2426; Acciari et al. 2020), in our sample that was observed by MAGIC but not listed in TeVCat. Finally, we compile a sample of 58 sources (49 BL Lacs, seven FSRQs, and two BCUs), of which 48 sources (44 BL Lacs, two FSRQs, and two BCUs) are in a quiescent state

and 21 sources (14 BL Lacs and seven FSRQs) are in a flaring state. These sources are listed in Tables 1 and 2, respectively.

2.1. The Extragalactic Background Light Correction

The VHE spectrum of our sample is reduced by the EBL attenuation, leading to difficulty obtaining the deabsorbed spectrum information directly. For this reason, we try to correct the absorbed spectrum.

Assuming the absorbed VHE spectrum of a TeV blazar forms a power-law function:

$$\frac{dN}{dE_{\text{abs}}} = N_{0,\text{abs}} \times \left(\frac{E}{E_0} \right)^{-\Gamma_{\text{abs}}}, \quad (1)$$

where Γ_{abs} is the photon spectral index in the VHE spectrum, E_0 is the normalization energy, and $N_{0,\text{abs}}$ is the differential photon flux at E_0 in units of $\text{cm}^{-2} \text{s}^{-1} \text{TeV}^{-1}$. Then, the deabsorbed spectrum can be obtained by the following function:

$$\frac{dN}{dE_{\text{deabs}}} = \frac{dN}{dE_{\text{abs}}} e^{\tau(E,z)} = N_{0,\text{deabs}} \times \left(\frac{E}{E_0} \right)^{-\Gamma_{\text{deabs}}}, \quad (2)$$

where $\tau(E, z)$, the optical depth, is a function of redshift and energy, $N_{0,\text{deabs}}$ (hereafter N_0) is the differential photon flux at E_0 , and Γ_{deabs} (hereafter Γ) is the photon spectral index with EBL deabsorption. The model from Franceschini et al. (2008) is used to correct the VHE spectrum, and then the deabsorbed spectrum information can be obtained. We consider the flux in the TeV band in units of $\text{TeV cm}^{-2} \text{s}^{-1}$, which can be calculated by

$$F = E^2 \times \frac{dN}{dE_{\text{deabs}}}, \quad (3)$$

where here E is 1 TeV. Meanwhile, we show the absorbed (original) spectrum and the deabsorbed spectrum in the Appendix for the quiescent state and the flaring state.

The isotropic TeV γ -ray luminosity, in units of erg s^{-1} , is expressed as

$$L = 4\pi d_L^2 (1+z)^{\Gamma-2} F, \quad (4)$$

here $(1+z)^{\Gamma-2}$ stands for a K -correction, z is the redshift, Γ is the photon spectral index with EBL deabsorption, F is the TeV γ -ray flux, and d_L represents the luminosity distance, expressed by $d_L = \frac{(1+z)c}{H_0} \int_z^{1+z} \frac{1}{\sqrt{\Omega_M x^3 + 1 - \Omega_M}} dx$. We calculate the deabsorbed TeV γ -ray luminosity ($L_{1 \text{ TeV, de-abs}}$, hereafter $L_{1 \text{ TeV}}^{\text{ob}}$) at 1 TeV for the sources in our sample.

3. Results

The blazar sequence is reflected in the diagrams as an anticorrelation between luminosity in different bands and synchrotron peak frequency (Fossati et al. 1998; Nieppola et al. 2006, 2008; Giommi et al. 2012a, 2012b; Mao et al. 2016; Fan et al. 2017; Yang et al. 2022b). Therefore, we can test the blazar sequence in the TeV band by studying the correlation between the TeV luminosity and synchrotron peak frequency.

In order to evaluate the correlation, a Pearson correlation analysis was used in this work. This analysis presents the results in two parameters, namely correlation coefficient (r) and

Table 1
Sample of 48 TeV Blazars in the Quiescent State

TeV Name (1)	Other Name (2)	z (3)	Class (4)	$\log \nu_p^{\text{ob}}$ (5)	δ (6)	$N_{0,\text{abs}}$ (7)	$\Delta N_{0,\text{abs}}$ (8)	Γ_{abs} (9)	$\Delta \Gamma_{\text{abs}}$ (10)	E_0 (11)	N_0 (12)	ΔN_0 (13)	Γ (14)	$\Delta \Gamma$ (15)	E_0 (16)	References (17)
TeV J0013-188	SHBL J001355.9-185406	0.094	B	14.96	29	1.20E-12	2.09E-14	3.43	0.05	0.51	1.94E-12	5.98E-14	2.78	0.08	0.51	H. E. S. S. Collaboration et al. (2013a)
TeV J0033-193	KUV 00311-1938	0.61	B	16.81	13.2	3.14E-11	3.00E-27	4.39	2.60E-16	0.17	8.37E-11	1.47E-26	1.92	4.77E-16	0.17	Abdalla et al. (2020)
TeV J0112+227	S2 0109+22	0.265	B	13.90	53.4	1.56E-10	1.86E-11	3.39	0.22	0.16	4.84E-10	7.47E-11	3.03	0.35	0.12	MAGIC Collaboration et al. (2018a)
TeV J0152+017	RGB J0152+017	0.08	B	15.73	24.8	6.24E-13	5.81E-14	2.95	0.12	1	1.34E-12	1.14E-13	2.43	0.11	1	Aharonian et al. (2008)
TeV J0214+517	TXS 0210+515	0.049	B	15.92	4.7	1.32E-13	3.28E-15	1.95	0.03	1.574	2.38E-13	1.47E-15	1.65	0.01	1.574	Acciari et al. (2020)
TeV J0222+430	3C 66A	0.444	B	14.96	36	1.67E-11	2.24E-12	3.08	0.18	0.3	2.48E-10	2.49E-11	0.67	0.10	0.3	Aliu et al. (2009)
TeV J0232+202	1ES 0229+200	0.139	B	16.26	14.2	6.74E-13	9.44E-14	2.51	0.15	1	2.70E-12	4.08E-13	1.44	0.20	1	Aharonian et al. (2007a)
TeV J0303-241	PKS 0301-243	0.2657	B	16.10	16.4	1.09E-11	1.85E-12	4.48	0.62	0.29	2.27E-11	2.83E-12	2.95	0.47	0.29	H. E. S. S. Collaboration et al. (2013b)
TeV J0319+187	RBS 0413	0.19	B	16.98	3.7	1.37E-11	1.11E-12	3.18	0.15	0.3	2.10E-11	8.82E-13	1.89	0.08	0.3	Aliu et al. (2012)
TeV J0349-119	1ES 0347-121	0.188	B	17.47	14.3	4.52E-13	6.97E-14	3.10	0.18	1	3.27E-12	4.29E-13	1.81	0.16	1	Aharonian et al. (2007b)
TeV J0416+010	1ES 0414+009	0.287	B	17.61	2	5.54E-12	6.33E-13	3.29	0.15	0.305	1.59E-11	2.91E-12	1.50	0.25	0.305	H. E. S. S. Collaboration et al. (2012a)
TeV J0449-438	PKS 0447-439	0.205	U	13.08	...	2.81E-13	1.13E-13	3.99	0.44	1	2.53E-12	9.81E-13	2.57	0.43	1	H. E. S. S. Collaboration et al. (2013c)
TeV J0509+056	TXS 0506+056	0.3365	B	14.43	...	6.42E-11	1.16E-11	4.81	0.91	0.15	8.20E-11	1.68E-11	4.05	1.05	0.15	Abeysekara et al. (2018)
TeV J0521+211	VER J0521+211	0.108	B	15.24	14.3	1.99E-11	1.27E-12	3.46	0.14	0.4	3.08E-11	1.70E-12	2.83	0.13	0.4	Archambault et al. (2013)
TeV J0648+152	RX J0648.7+1516	0.179	B	17.07	6.7	2.32E-11	2.71E-12	4.37	0.43	0.3	3.74E-11	4.30E-12	3.48	0.43	0.3	Aliu et al. (2011)
TeV J0710+591	RGB J0710+591	0.125	B	17.25	1.5	5.58E-12	1.03E-12	2.70	0.20	0.5	1.08E-11	2.16E-12	1.88	0.22	0.5	Acciari et al. (2010a)
TeV J0809+523	1ES 0806+524	0.138	B	16.26	3.7	3.90E-12	7.56E-13	2.77	0.25	0.5	7.77E-12	2.33E-12	2.18	0.41	0.5	Aleksić et al. (2015)
TeV J0847+115	RBS 723	0.198	B	16.37*	1.9	1.10E-11	2.00E-12	3.76	0.71	0.3	1.84E-11	3.96E-12	2.93	0.86	0.3	Acciari et al. (2020)
TeV J0854+201	OJ 287	0.3056	B	13.62	67.5	3.20E-11	6.45E-12	2.24	0.29	0.1	3.53E-11	1.23E-11	1.56	0.50	0.1	Seta et al. (2009)
TeV J1010-313	1RXS J101015.9-311909	0.142639	B	16.26	45.8	2.04E-13	8.68E-14	3.00	0.46	1	8.71E-13	3.71E-13	2.06	0.47	1	H. E. S. S. Collaboration et al. (2012b)
TeV J1015+494	1ES 1011+496	0.212	B	16.68	1.3	1.97E-10	3.47E-11	4.11	0.51	0.2	2.60E-10	5.50E-11	3.56	0.67	0.2	Albert et al. (2007)
TeV J1103-234	1ES 1101-232	0.186	B	17.07	1.4	5.52E-13	7.95E-14	2.94	0.19	1	3.92E-12	4.90E-13	1.68	0.16	1	Aharonian et al. (2007c)
	Mkn 421	0.031	B	16.61	1.5	1.58E-10	1.48E-11	2.89	0.19	0.3	1.70E-10	1.58E-11	2.74	0.19	0.3	Baloković et al. (2016)

Table 1
(Continued)

TeV Name (1)	Other Name (2)	z (3)	Class (4)	$\log \nu_p^{\text{ob}}$ (5)	δ (6)	$N_{0,\text{abs}}$ (7)	$\Delta N_{0,\text{abs}}$ (8)	Γ_{abs} (9)	$\Delta \Gamma_{\text{abs}}$ (10)	E_0 (11)	N_0 (12)	ΔN_0 (13)	Γ (14)	$\Delta \Gamma$ (15)	E_0 (16)	References (17)
TeV																
J1104+382																
TeV J1136+701	Mkn 180	0.045	B	16.72	1.4	4.27E-11	2.58E-12	3.16	0.08	0.3	4.75E-11	3.90E-12	2.91	0.11	0.3	Albert et al. (2006)
TeV J1217+301	1ES 1215+303	0.131	B	15.35	15.1	1.53E-11	1.28E-12	3.29	0.16	0.4	2.66E-11	2.27E-12	2.61	0.17	0.4	Valverde et al. (2020)
TeV J1221+282	W Comae	0.103	B	15.54	13.8	7.35E-12	7.10E-13	3.06	0.21	0.5	1.26E-11	1.23E-12	2.38	0.22	0.5	Acciari et al. (2009a)
TeV J1221+301	1ES 1218+304	0.182	B	17.37	...	1.15E-11	7.81E-13	3.07	0.10	0.5	3.39E-11	1.76E-12	1.98	0.08	0.5	Acciari et al. (2010b)
TeV J1315-426	1ES 1312-423	0.105	B	16.44	...	2.40E-13	2.51E-14	2.68	0.15	1	6.68E-13	7.73E-14	2.00	0.17	1	H. E. S. S. Collaboration et al. (2013)
TeV J1422+323	B2 1420+32	0.682	F	13.63	4.3	1.04E-09	4.23E-11	4.19	0.09	0.1	1.70E-09	2.52E-10	3.31	0.36	0.1	MAGIC Collaboration et al. (2021)
TeV J1427+238	PKS 1424+240	0.16	B	16.26	34.8	5.01E-11	4.67E-12	3.85	0.27	0.2	6.05E-11	6.62E-12	3.32	0.34	0.2	Acciari et al. (2010c)
TeV J1428+426	1ES 1426+428	0.129	B	17.35	2.5	2.47E-11	3.69E-12	2.50	0.16	0.242	3.29E-11	3.62E-12	1.84	0.13	0.242	Acciari et al. (2020)
TeV J1443+120	1ES 1440+122	0.16306	B	16.97	1.5	1.50E-12	3.24E-13	3.09	0.44	0.5	3.75E-12	8.12E-13	2.10	0.46	0.5	Archambault et al. (2016)
TeV J1443-391	PKS 1440-389	0.065	B	16.33	...	3.10E-11	4.75E-12	3.38	0.27	0.274	3.63E-11	4.97E-12	3.05	0.25	0.274	Abdalla et al. (2020)
TeV J1512-091	PKS 1510-089	0.361	F	13.93	10.5	7.73E-11	4.17E-12	3.05	0.10	0.175	1.22E-10	2.07E-11	2.42	0.35	0.175	MAGIC Collaboration et al. (2018b)
TeV J1517-243	AP Librae	0.048	B	14.12	20.9	4.00E-12	4.96E-13	2.73	0.18	0.45	5.02E-12	6.07E-13	2.47	0.18	0.45	H. E. S. S. Collaboration et al. (2015)
TeV J1555+111	PG 1553+113	0.36	B	16.33	11.4	5.19E-11	6.38E-12	4.22	0.30	0.3	1.77E-10	1.60E-11	2.55	0.23	0.3	Aliu et al. (2015)
TeV J1653+397	Mkn 501	0.034	B	16.81	2.3	1.74E-10	1.04E-11	2.48	0.06	0.3	1.86E-10	1.09E-11	2.28	0.06	0.3	Ahnen et al. (2017)
TeV J1725+118	H 1722+119	0.4	B	16.35	14.3	4.21E-11	8.10E-12	3.56	0.24	0.2	8.24E-11	2.96E-11	2.83	0.51	0.2	Ahnen et al. (2016a)
TeV J1743+196	1ES 1741+196	0.084	B	15.54	17.3	9.28E-12	2.39E-13	2.70	0.10	0.3	1.12E-11	4.43E-13	2.36	0.15	0.3	Abeysekara et al. (2016)
TeV J1943+213	HESS J1943+213	0.16	U	16.66	...	9.61E-12	5.81E-13	2.81	0.10	0.4	3.24E-11	2.82E-12	1.81	0.13	0.3	Archer et al. (2018)
TeV J1959+651	1ES 1959+650	0.047	B	17.32	...	2.67E-12	2.28E-13	2.54	0.11	1	4.13E-12	3.80E-13	2.25	0.12	1	Tagliaferri et al. (2008)
TeV J2009-488	PKS 2005-489	0.071	B	16.63	6.7	1.34E-11	1.78E-12	3.20	0.17	0.4	1.70E-11	2.14E-12	2.71	0.16	0.4	H. E. S. S. Collaboration et al. (2010a)
TeV J2039+523	1ES 2037+521	0.053	B	15.82	53	6.40E-12	1.13E-13	2.27	0.02	0.4	8.06E-12	1.37E-13	1.99	0.02	0.4	Acciari et al. (2020)
TeV J2158-302	PKS 2155-304	0.116	B	16.25	11.1	1.83E-12	1.05E-13	3.53	0.05	1	5.30E-12	3.86E-13	2.88	0.06	1	H. E. S. S. Collaboration et al. (2010b)
TeV J2250+384	B3 2247+381	0.1187	B	16.55	25.7	1.36E-11	1.17E-12	3.31	0.13	0.3	1.94E-11	1.79E-12	2.69	0.14	0.3	Aleksić et al. (2012)
	1ES 2344+514	0.044	B	16.62	2.7	2.64E-12	1.77E-13	2.49	0.08	0.91	3.88E-12	2.40E-13	2.20	0.07	0.91	Allen et al. (2017)

Table 1
(Continued)

TeV Name (1)	Other Name (2)	z (3)	Class (4)	$\log \nu_p^{\text{ob}}$ (5)	δ (6)	$N_{0,\text{abs}}$ (7)	$\Delta N_{0,\text{abs}}$ (8)	Γ_{abs} (9)	$\Delta \Gamma_{\text{abs}}$ (10)	E_0 (11)	N_0 (12)	ΔN_0 (13)	Γ (14)	$\Delta \Gamma$ (15)	E_0 (16)	References (17)
TeV																
J2347+517																
TeV	H 2356-309	0.165	B	16.67	14.3	3.50E-13	4.55E-14	2.97	0.15	1	1.89E-12	2.03E-13	1.89	0.12	1	H. E. S. S. Collaboration et al. (2010c)
J2359-306																
4FGL	RGB	0.104	B	16.74	15.2	2.61E-12	3.00E-13	2.31	0.13	0.379	4.11E-12	6.31E-13	1.76	0.18	0.379	Acciari et al. (2020)
J2042.1	J2042.1+2426															
+2427																

Note. Col. (1): TeV name; col. (2): other name; col. (3): redshift; col. (4): classification, “B” for BLL, “F” for FSRQ, and “U” for BCU; col. (5): synchrotron peak frequency; TeV J0847+115 is from Fan et al. (2016) and the others are from Yang et al. (2022a); col. (6): Doppler factor from Chen (2018); col. (7): the absorbed normalization in units of $\text{cm}^{-2} \text{s}^{-1} \text{TeV}^{-1}$; col. (8): the error of the absorbed normalization in units of $\text{cm}^{-2} \text{s}^{-1} \text{TeV}^{-1}$; col. (9): the absorbed photon index; col. (10): the error of the absorbed photon index; col. (11): the normalization energy in units of TeV; col. (12): the deabsorbed normalization in units of $\text{cm}^{-2} \text{s}^{-1} \text{TeV}^{-1}$; col. (13): the error of the deabsorbed normalization in units of $\text{cm}^{-2} \text{s}^{-1} \text{TeV}^{-1}$; col. (14): the deabsorbed photon index; col. (15): the error of the deabsorbed photon index; col. (16): the normalization energy in units of TeV; col. (17): reference of the TeV spectra. The “–” symbol indicates a null value.

Table 2
Sample of 21 TeV Blazars in the Flaring State

TeV Name (1)	Other Name (2)	z (3)	Class (4)	$\log \nu_p^{\text{ob}}$ (5)	δ (6)	$N_{0,\text{abs}}$ (7)	$\Delta N_{0,\text{abs}}$ (8)	Γ_{abs} (9)	$\Delta \Gamma_{\text{abs}}$ (10)	E_0 (11)	N_0 (12)	ΔN_0 (13)	Γ (14)	$\Delta \Gamma$ (15)	E_0 (16)	References (17)
TeV J0112+227	S2 0109+22	0.265	B	13.90	53.4	1.62E-09	5.92E-11	3.57	0.09	0.11	1.38E-09	7.38E-12	3.28	0.01	0.12	MAGIC Collaboration et al. (2018a)
TeV J0218+359	S3 0218+35	0.944	F	12.99	...	2.18E-09	2.17E-10	3.91	0.45	0.1	4.28E-09	7.75E-10	2.45	0.89	0.1	Ahnen et al. (2016b)
TeV J0521+211	VER J0521+211	0.108	B	15.24	14.3	2.35E-10	1.96E-11	3.16	0.12	0.3	3.32E-10	1.44E-11	2.72	0.07	0.3	Adams et al. (2022a)
TeV J0721+713	S5 0716+714	0.31	B	14.42	20.3	1.23E-09	7.35E-11	4.65	0.16	0.15	1.47E-09	1.27E-10	3.65	0.24	0.15	MAGIC Collaboration et al. (2018c)
TeV J0809+523	1ES 0806+524	0.138	B	16.26	3.7	1.27E-11	1.65E-12	2.92	0.19	0.5	2.75E-11	2.93E-12	2.19	0.16	0.5	Aleksić et al. (2015)
TeV J0854+201	OJ 287	0.3056	B	13.62	67.5	1.48E-11	1.15E-12	2.18	0.11	0.1	1.59E-11	3.76E-12	1.42	0.33	0.1	Seta et al. (2009)
TeV J0958+655	S4 0954+65	0.367	B	14.04	26.5	1.01E-09	5.63E-11	4.64	0.24	0.15	1.38E-09	2.86E-11	3.98	0.09	0.15	MAGIC Collaboration et al. (2018d)
TeV J1104+382	Mkn 421	0.031	B	16.61	1.5	2.49E-11	1.24E-12	2.28	0.06	1	3.31E-11	1.71E-12	2.09	0.06	1	Acciari et al. (2009b)
TeV J1159+292	Ton 599	0.7247	F	13.54	29.3	3.08E-10	1.76E-11	4.37	0.13	0.2	1.56E-09	3.15E-10	0.16	0.61	0.2	Adams et al. (2022b)
TeV J1217+301	1ES 1215+303	0.131	B	15.35	15.1	9.42E-11	6.82E-12	3.59	0.14	0.4	8.49E-11	6.77E-12	2.93	0.12	0.5	Valverde et al. (2020)
TeV J1221+282	W Comae	0.103	B	15.54	13.8	2.11E-11	3.23E-12	3.72	0.37	0.4	3.19E-11	4.39E-12	3.11	0.35	0.4	Acciari et al. (2008)
TeV J1224+213	4C +21.35	0.435	F	14.06	11.3	7.85E-10	9.37E-11	3.73	0.21	0.2	1.85E-09	5.69E-11	2.63	0.06	0.2	Aleksić et al. (2011)
6	TeV J1256-057	3C 279	F	12.79	27.7	4.45E-10	1.08E-10	4.33	0.44	0.2	8.66E-10	5.20E-10	3.75	1.03	0.2	MAGIC Collaboration et al. (2008)
TeV J1422+323	B2 1420+32	0.682	F	13.63	4.3	2.41E-09	2.35E-10	4.12	0.18	0.1	3.75E-09	5.15E-10	3.49	0.27	0.1	MAGIC Collaboration et al. (2021)
TeV J1443+250	PKS 1441+25	0.93978	F	13.99	...	1.13E-09	1.14E-10	4.63	0.24	0.1	2.59E-09	1.25E-10	3.16	0.14	0.1	Ahnen et al. (2015)
TeV J1512-091	PKS 1510-089	0.361	F	13.93	10.5	3.27E-10	5.10E-11	4.22	0.18	0.265	8.46E-10	8.63E-11	3.34	0.13	0.265	H. E. S. S. Collaboration et al. (2021)
TeV J1653+397	Mn 501	0.034	B	16.81	2.3	6.32E-10	4.56E-11	2.26	0.07	0.3	6.76E-10	4.95E-11	2.06	0.07	0.3	Ahnen et al. (2017)
TeV J1728+502	1ES 1727+502	0.055	B	16.52	2	7.71E-12	9.10E-13	2.19	0.24	0.62	1.09E-11	1.30E-12	1.82	0.24	0.62	Archambault et al. (2015)
TeV J2202+422	BL Lacertae	0.069	B	13.93	3.8	5.55E-10	7.96E-11	3.69	0.48	0.3	6.50E-10	9.07E-11	3.38	0.47	0.3	Arlen et al. (2013)
TeV J2243+203	RGB J2243+203	0.39	B	15.14	14.3	6.33E-10	4.79E-11	4.62	0.24	0.15	8.69E-10	1.05E-10	3.44	0.44	0.15	Abeysekara et al. (2017)
TeV J2347+517	1ES 2344+514	0.044	B	16.62	2.7	1.73E-11	1.27E-12	2.44	0.14	1	2.61E-11	1.83E-12	2.14	0.13	1	Acciari et al. (2011)

Note. Col. (1): TeV name; col. (2): other name; col. (3): redshift; col. (4): classification, “B” for BLL and “F” for FSRQ; col. (5): synchrotron peak frequency from Yang et al. (2022a); col. (6): Doppler factor from Chen (2018); col. (7): the absorbed normalization in units of $\text{cm}^{-2} \text{s}^{-1} \text{TeV}^{-1}$; col. (8): the error of the absorbed normalization in units of $\text{cm}^{-2} \text{s}^{-1} \text{TeV}^{-1}$; col. (9): the absorbed photon index; col. (10): the error of the absorbed photon index; col. (11): the normalization energy in units of TeV; col. (12): the deabsorbed normalization in units of $\text{cm}^{-2} \text{s}^{-1} \text{TeV}^{-1}$; col. (13): the error of the deabsorbed normalization in units of $\text{cm}^{-2} \text{s}^{-1} \text{TeV}^{-1}$; col. (14): the deabsorbed photon index; col. (15): the error of the deabsorbed photon index; col. (16): the normalization energy in units of TeV; col. (17): reference of the TeV spectra. The “–” symbol indicates a null value.

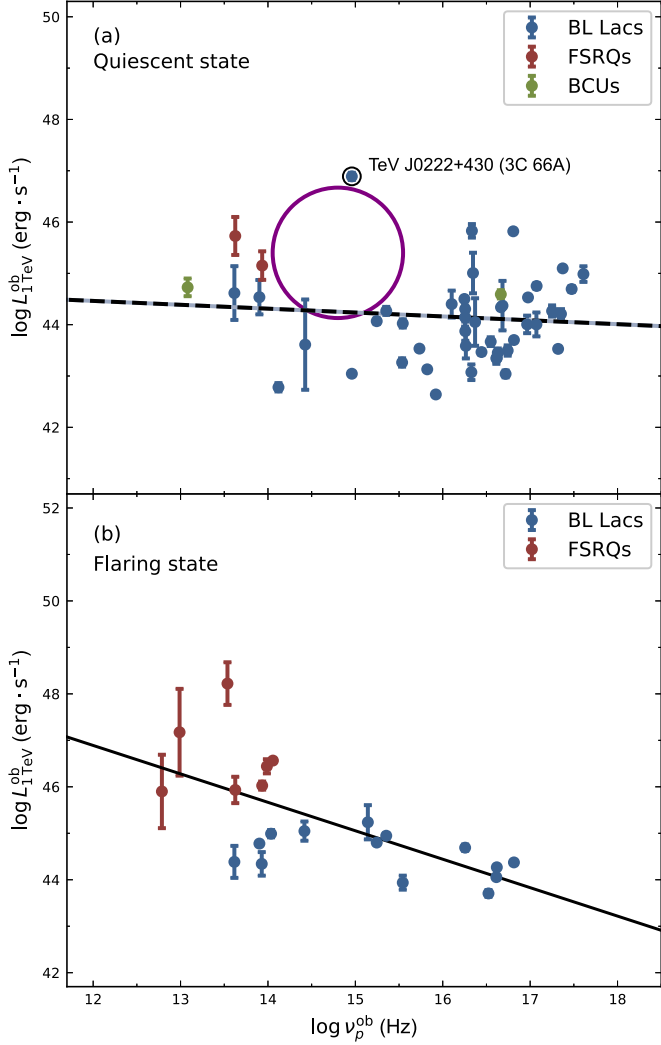


Figure 1. The observed correlation between $\log L_1^{\text{ob}} \text{TeV}$ and $\log \nu_p^{\text{ob}}$ in both (a) a quiescent state and (b) a flaring state. The blue circle denotes BL Lacs, the red FSRQs, and the green BCUs. The solid line represents the corresponding linear regression for the whole sample. The violet circle represents the particular region to be discussed in Section 5, and the dashed line indicates the trend of the correlation.

chance probability (p). The coefficient r , the most common way of measuring a linear correlation, is a number between -1 and 1 that measures the strength and direction of the relationship between two variables. If the p -value is smaller than a critical value, which is usually set as 0.05 , then the relationship is statistically significant and allows one to reject the null hypothesis, in which the two variables are not correlated. In addition, a least-squares linear regression was applied to find the linear correlation.

3.1. The Observed Correlation between TeV Luminosity and Synchrotron Peak Frequency

Quiescent state. Based on the obtained TeV luminosity and synchrotron peak frequency, we plot $\log L_1^{\text{ob}} \text{TeV}$ versus $\log \nu_p^{\text{ob}}$ in the top panel of Figure 1. When the Pearson correlation analysis is applied to test the correlation, we find that there is no significant correlation between $\log L_1^{\text{ob}} \text{TeV}$ and $\log \nu_p^{\text{ob}}$ due to $r = -0.1$ and $p = 50.39\%$ for the case of TeV blazars in the

quiescent state. However, we can still see that there is a trend of anticorrelation between the two parameters in this panel, which reveals the existence of a blazar sequence because some ISP TeV sources are absent in the circled region; this will be discussed in Section 5.

Flaring state. Compared to the quiescent state, we find an anticorrelation between $\log L_1^{\text{ob}} \text{TeV}$ and $\log \nu_p^{\text{ob}}$ in the flaring state and present a linear regression:

$$\log L_1^{\text{ob}} \text{TeV} = -(0.61 \pm 0.15) \log \nu_p^{\text{ob}} + (54.23 \pm 2.27), \quad (5)$$

with $r = 0.67$ and $p = 7.95 \times 10^{-4}$, as shown in the lower panel of Figure 1. This result suggests a strong anticorrelation between TeV luminosity and the synchrotron peak frequency in the flaring state, and indicates that the blazar sequence is present more obvious in the flaring state than in the quiescent state for TeV blazars.

3.2. The Intrinsic Correlation between TeV Luminosity and Synchrotron Peak Frequency

In a relativistic beaming model, the observed flux density, f^{ob} , and the intrinsic one, f^{in} , exist in a correlation, $f^{\text{ob}} = \delta^q f^{\text{in}}$ ($\delta = [\gamma_{\text{bulk}}(1 - \beta_{\text{bulk}} \cos \theta)]^{-1}$, where δ is the Doppler factor, β_{bulk} is the bulk velocity, θ is the viewing angle, and γ_{bulk} is the bulk Lorentz factor); then, the intrinsic luminosity (L^{in}) and frequency (ν^{in}) can be calculated through the observed luminosity (L^{ob}) and frequency (ν^{ob}):

$$L^{\text{in}} = \frac{L^{\text{ob}}}{\delta^{q+1}}, \quad \nu^{\text{in}} = \frac{\nu^{\text{ob}}}{\delta/(1+z)}, \quad (6)$$

where $q = 2 + \alpha$ for a continuous jet, $q = 3 + \alpha$ for a spherical jet, and α is the spectral index ($f_v \propto \nu^{-\alpha}$, $\alpha = \Gamma - 1$; Lind & Blandford 1985). We compile the Doppler factors from Chen (2018); the values range from 1.3 to 67.5 for the quiescent state and from 1.6 to 67.5 for the flaring state in our sample. We calculate the intrinsic TeV luminosity $L_1^{\text{in}} \text{TeV}$ at 1 TeV for the sources in our sample with available Doppler factor for both states. The remaining sources with unavailable Doppler factors are excluded in the analysis of the intrinsic correlation.

Quiescent state. The top panel of Figure 2 shows a positive correlation between the intrinsic TeV luminosity and the synchrotron peak frequency in the quiescent state. We obtain

$$\log L_1^{\text{in}} \text{TeV} = (1.20 \pm 0.21) \log \nu_p^{\text{in}} + (21.86 \pm 3.23), \quad (7)$$

with $r = 0.67$ and $p < 10^{-4}$ for the case of $q = \alpha + 2$, and

$$\log L_1^{\text{in}} \text{TeV} = (1.49 \pm 0.24) \log \nu_p^{\text{in}} + (16.54 \pm 3.66), \quad (8)$$

with $r = 0.71$ and $p < 10^{-4}$ for the case of $q = \alpha + 3$.

Flaring state. The lower panel of Figure 2 also shows a positive correlation between the intrinsic TeV luminosity and the synchrotron peak frequency in the flaring state. We obtain

$$\log L_1^{\text{in}} \text{TeV} = (0.86 \pm 0.34) \log \nu_p^{\text{in}} + (28.27 \pm 4.72), \quad (9)$$

with $r = 0.53$ and $p = 2.02\%$ for the case of $q = \alpha + 2$, and

$$\log L_1^{\text{in}} \text{TeV} = (1.13 \pm 0.36) \log \nu_p^{\text{in}} + (23.61 \pm 5.05), \quad (10)$$

with $r = 0.60$ and $p = 6.17 \times 10^{-3}$ for the case of $q = \alpha + 3$.

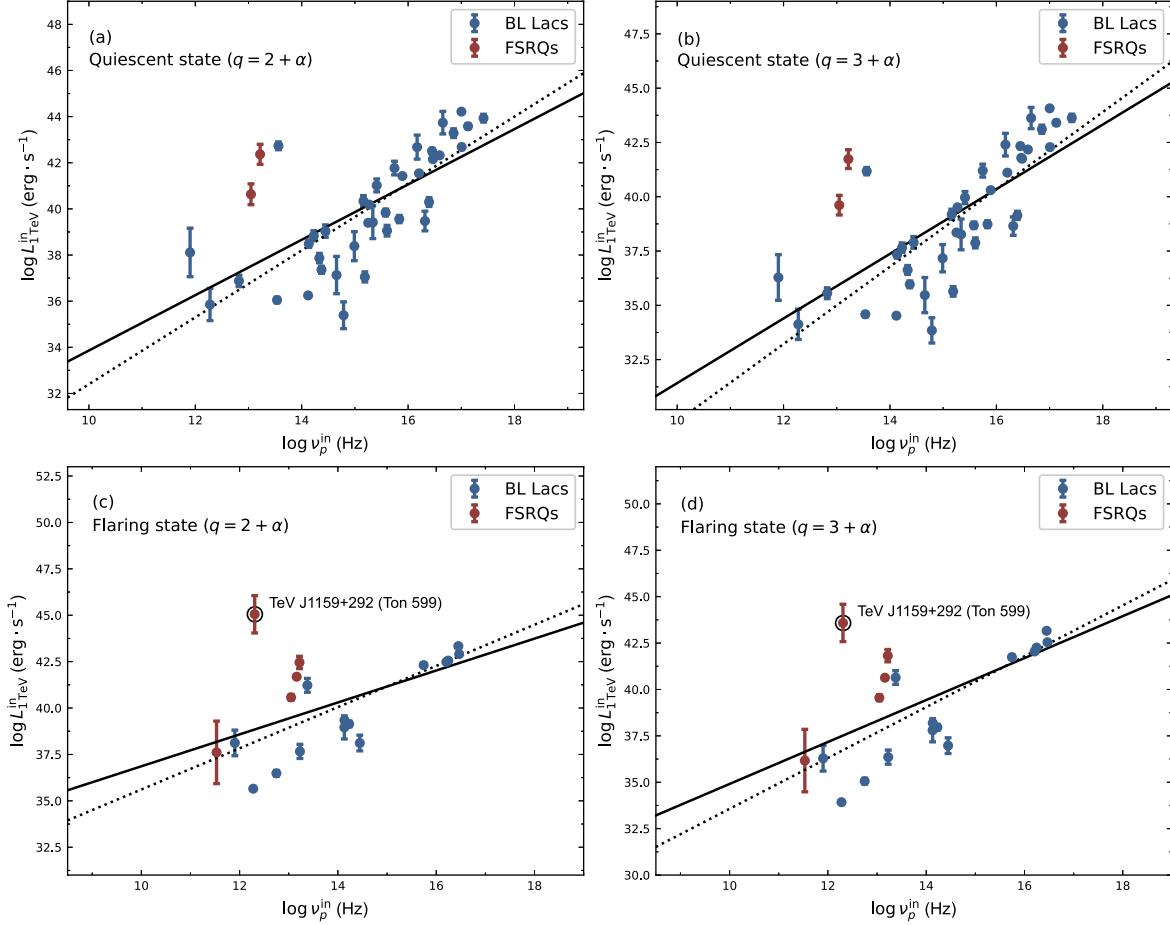


Figure 2. The intrinsic correlation between $\log L_1^{\text{in}}$ and $\log \nu_p^{\text{in}}$ in both (a, b) a quiescent state and (c, d) a flaring state. (a) and (c) show the cases for $q = 2 + \alpha$, and (b) and (d) show the cases for $q = 3 + \alpha$. The blue circle denotes BL Lacs, and the red FSRQs. The solid lines represent the corresponding linear regression for the whole sample. The dotted lines will be discussed in Section 5.

From the intrinsic relationship, we note that the intrinsic TeV luminosity and synchrotron peak frequency show a very strong positive correlation in both quiescent and flaring states. Thus, we suggest that the blazar sequence is not present in the TeV band after removing the beaming effect. As abovementioned, we notice the absence (or only a trend) of the blazar sequence for the quiescent state and the presence of a significant blazar sequence for the flaring state in Figure 1. Moreover, the flatter slopes of the intrinsic diagrams for the flaring state than that for the quiescent state in Figure 2 indicate a stronger beaming effect for the flaring state. We shall discuss this issue in Section 4.

4. Comparison of Fermi γ -Ray Emission between the Quiescent State and Flaring State

In order to investigate whether a stronger beaming effect results in (or boosts) the presence of the blazar sequence in the flaring state, we try to compare the γ -ray emission between the quiescent state and flaring state for the sources in our sample. Previous studies have found that the bulk Lorentz factor (or the Doppler factor, $\delta \approx \gamma_{\text{bulk}}$ for a blazar) shows a strong correlation with γ -ray emission for Fermi-detected AGNs (Fan et al. 2014b; Ghisellini et al. 2014; Blandford et al. 2019; Zhang et al. 2020). Therefore, the γ -ray emission can be considered to be an indicator of the beaming effect.

4.1. Introduction to Fermi-LAT and Data Analysis

The Fermi-LAT¹⁰ detects γ -rays in the energy band from 20 MeV to beyond 300 GeV and surveys the entire sky every day (Atwood et al. 2009). In order to obtain the GeV γ -ray emission in the quiescent state and flaring state, we analyze Fermi data in the same observation periods when the VHE observations are performed. We use MJD 57863 as the starting time of the data for analysis if the VHE observation period encompasses a campaign before the launch of the Fermi-LAT. For TeV J1443+120, for instance, the observation period spans the months of 2008 May and 2010 June, totaling 53 hr; we then choose MJD 57863 as its start time. We perform a binned likelihood analysis of the data using the latest LAT Fermi tools¹¹ 2.2.0 and the instrument response functions P8R3_SOURCE_V3.¹² The energy of the data ranges from 0.1 to 300 GeV, and we select the maximum zenith angle value as 90° to reduce the photons coming from the Earth's limb. The condition “evclass = 128, evtype = 3” is used to filter events with a high probability of being photons. For each source, the region of interest considered is a circle of 10° radius surrounding the catalog source position. The condition

¹⁰ <https://fermi.gsfc.nasa.gov>

¹¹ <https://fermi.gsfc.nasa.gov/ssc/data/analysis/>

¹² https://fermi.gsfc.nasa.gov/ssc/data/analysis/documentation/Cicerone/Cicerone_LAT_IRFs/IRF_overview.html

Table 3
Normalizations and Parameters of the Spectrum in the Quiescent State

TeV Name (1)	N_0 (2)	ΔN_0 (3)	Γ (4)	$\Delta \Gamma$ (5)	β (6)	$\Delta \beta$ (7)	E_0 (8)	Observation Periods (9)
TeV J0013-188 ^a	7.6E-14	3.18E-14	1.71	0.26	2498.28394	MJD 54683–55912
TeV J0033-193	1.36E-12	1.77E-13	1.74	0.11	0.10	0.06	1571.1472	MJD 55145–56954
TeV J0112+227	3.29E-11	7.19E-12	1.71	0.26	0.06	0.10	755.25354	MJD 57225–57231
TeV J0214+517 ^a	3.71E-14	1.75E-14	1.66	0.32	4042.61401	MJD 57370–58042
TeV J0303-241	4.35E-12	7.08E-13	2.06	0.13	0.01	0.06	945.1168	MJD 55044–55895
TeV J0319+187 ^a	1.51E-14	8.52E-15	1.43	0.31	6216.29443	MJD 54732–55485
TeV J0416+010 ^a	4.16E-14	5.19E-15	1.67	0.07	3730.71851	MJD 54683–55158
TeV J0449-438	4.52E-12	4.03E-13	1.87	0.08	0.03	0.04	1581.183	MJD 55136–55227
TeV J0509+056	2.04E-11	1.46E-12	2.09	0.05	0.06	0.03	1074.2167	MJD 58019.39–58155.18
TeV J0521+211	5.43E-12	9.49E-15	1.81	1.23E-03	0.01	4.33E-04	1542.1824	MJD 55126–55212
TeV J0648+152 ^a	1.54E-14	3.87E-15	2.92	0.09	4960.08594	MJD 55259–55301
TeV J0710+591 ^a	3.68E-14	1.4E-14	1.50	0.23	4958.52441	MJD 54801–54921
TeV J0809+523	1.88E-12	3.46E-13	2.27	0.14	2.13E-06	1.16E-03	1345.8887	MJD 55568–55622
TeV J1217+301	6.85E-12	6.52E-14	1.82	0.01	0.06	3.28E-03	1093.8949	MJD 57202–57562
TeV J1221+301 ^a	2.09E-13	3.53E-14	1.54	0.11	4501.46387	MJD 54801–54952
TeV J1422+323	3.96E-10	1.24E-12	1.87	2.63E-03	0.04	1.08E-03	579.01245	MJD 58873.5–58880.5
TeV J1427+238	7.55E-12	5.36E-13	1.76	0.06	0.04	0.02	1204.567	MJD 54881–55003
TeV J1443+120 ^a	6.28E-14	1.68E-14	1.79	0.20	3828.12671	MJD 54683–55362
TeV J1443-391	7.18E-13	1.68E-13	1.25	0.15	0.20	0.07	1978.045	MJD 55985–56074
TeV J1512-091	7.26E-11	2.27E-12	2.45	0.02	0.02	0.01	723.6382	MJD 56000–58000
TeV J1517-243	8.55E-12	1.15E-12	2.32	0.12	6.77E-09	3.46E-05	811.1857	MJD 55326–55689
TeV J1555+111	4.86E-12	3.36E-13	1.66	0.05	0.07	0.03	1802.4828	MJD 55317–56108
TeV J1653+397	4.73E-12	4.49E-14	1.71	0.01	2.00E-10	5.10E-07	1486.4363	MJD 54907–55004
TeV J1743+196 ^a	2.7E-14	2.54E-14	1.25	0.37	2791.80957	MJD 54940–56834
TeV J2347+517	2.65E-13	2.21E-14	1.70	0.04	0.01	0.01	1934.7299	MJD 54683–57023

Notes. Col. (1): TeV name; col. (2): the normalization in units of $\text{cm}^{-2} \text{s}^{-1} \text{MeV}^{-1}$; col. (3): the error of normalization in units of $\text{cm}^{-2} \text{s}^{-1} \text{MeV}^{-1}$; col. (4): the photon index; col. (5): the error of the photon index; col. (6): the curvature index of the log-parabola function; col. (7): the error of the curvature index; col. (8): the pivot energy in units of MeV; col. (9): the same observation periods as the VHE observation. The “–” symbol indicates a null value.

^a Power-law function. The other sources are the log-parabola function.

“(DATA_QUAL ≥ 0)&&(LAT_CONFIG==1)” is used to select the good time intervals. The background model consists of the Galactic (gll_iem_v07.fits) and isotropic extragalactic diffuse emission models (iso_P8R3_SOURCE_V3_v1.txt).¹³ The normalizations of the two diffuse emission components are set as free parameters in the analysis. When performing the likelihood fitting, we fix the parameters of the least significant sources until convergence is reached.

The spectrum of each source is described with a log-parabola function:

$$\frac{dN}{dE} = N_0 \times \left(\frac{E}{E_0} \right)^{-\Gamma - \beta \log(\frac{E}{E_0})}, \quad (11)$$

where N_0 is the normalization in units of $\text{cm}^{-2} \text{s}^{-1} \text{MeV}^{-1}$, E_0 is the pivot energy, Γ is the photon index at E_0 , and β is the curvature index; or it is described with a power-law function:

$$\frac{dN}{dE} = N_0 \times \left(\frac{E}{E_0} \right)^{-\Gamma}, \quad (12)$$

where N_0 is the normalization in units of $\text{cm}^{-2} \text{s}^{-1} \text{MeV}^{-1}$, E_0 is the pivot energy, and Γ is the photon index. After we obtain the normalization and the parameters, the integral flux (F) in units of $\text{GeV cm}^{-2} \text{s}^{-1}$ can be expressed in the form

$$F = \int_{E_L}^{E_U} E \times \frac{dN}{dE} dE \quad (13)$$

¹³ <https://fermi.gsfc.nasa.gov/ssc/data/access/lat/BackgroundModels.html>

for the log-parabola or power-law functions. Here, E_L and E_U correspond to 1 GeV and 100 GeV, respectively. Then we calculate the γ -ray luminosity (L_γ) in units of erg s^{-1} through Equation (4).

4.2. Results and Conclusions Obtained from the Fermi-LAT Data Analysis

Finally, we obtain a sample of the Fermi γ -ray luminosity in the quiescent state and flaring state, with sample sizes of 25 (22 BL Lacs, two FSRQs, and one BCU) and 15 (nine BL Lacs and six FSRQs), respectively. We exclude the sources which were not significantly detected with a test statistic $\text{TS} < 9$ and/or model-predicted photons $N_{\text{pred}} < 8$ (Kapanadze & Gurchumelia 2022). The fitting normalizations and parameters of each source are listed in Tables 3 and 4. The Fermi γ -ray luminosity distributions of both the quiescent state and flaring state are shown in Figure 3. We compute the mean value of the γ -ray luminosity of both two states and get mean values of $\log L_{\gamma, \text{flaring}}^{\text{mean}} = 47.37 \pm 0.30 \text{ erg s}^{-1}$ and $\log L_{\gamma, \text{quiescent}}^{\text{mean}} = 45.51 \pm 0.24 \text{ erg s}^{-1}$, respectively. A Mann–Whitney U test is employed to compare the Fermi γ -ray luminosity distributions of these two states; the test gives a statistical value of 327.0 and a p -value smaller than 10^{-4} , which suggests that their mean values are different and the Fermi γ -ray luminosity of the flaring state is greater than that of the quiescent state. This result also reveals that blazars have a stronger beaming effect during the flaring state than during the quiescent state; therefore, we suggest the blazar sequence might be caused by

Table 4
Normalizations and Parameters of Spectrum in the Flaring State

TeV Name (1)	N_0 (2)	ΔN_0 (3)	Γ (4)	$\Delta \Gamma$ (5)	β (6)	$\Delta \beta$ (7)	E_0 (8)	Observation Periods (9)
TeV J0112+227	6.27E-11	2.67E-11	1.73	0.38	0.16	0.21	755.25354	MJD 57228
TeV J0218+359	5.86E-11	1.49E-11	1.30	0.23	0.30	0.13	764.40204	MJD 56863
TeV J0521+211	3.05E-11	7.51E-12	1.90	0.22	0.31	0.20	1542.1824	MJD 56628.5–56632.5
TeV J0721+713	1.34E-10	9.44E-12	1.86	0.05	0.03	0.03	734.5862	MJD 57040–57050
TeV J0809+523	1.39E-11	8.02E-12	2.14	0.49	0.14	0.30	1345.8887	MJD 55616
TeV J0958+655	3.94E-10	5.94E-11	1.83	0.14	0.11	0.08	651.3296	MJD 57067
TeV J1159+292	6.2E-10	6.11E-11	1.65	0.11	0.05	0.04	523.50714	MJD 58102–58104
TeV J1217+301	5.74E-11	2.13E-11	1.09	0.48	0.17	0.15	1093.8949	MJD 57844
TeV J1224+213	2.93E-09	2.49E-10	1.70	0.09	0.08	0.03	392.393	MJD 55364
TeV J1422+323 ^a	3.28E-10	2.66E-11	1.90	0.06	749.958679	MJD 58868.3–58870.3
TeV J1443+250	8.28E-11	8.22E-12	1.60	0.10	0.11	0.04	850.17804	MJD 57130–57139.5
TeV J1512-091	2.57E-10	4.75E-11	1.74	0.16	0.01	0.06	723.6382	MJD 57538
TeV J1653+397	9.38E-12	3.96E-12	1.48	0.27	0.05	0.10	1486.4363	MJD 54952.41–54955
TeV J2202+422	1.63E-10	4.12E-11	1.92	0.24	0.33	0.21	796.1543	MJD 55739.5–55740.5
TeV J2243+203	1.01E-11	5.48E-12	1.74	0.37	9.64E-09	3.98E-05	1517.4087	MJD 57012

Note. Col. (1): TeV name; col. (2): the normalization in units of $\text{cm}^{-2} \text{s}^{-1} \text{MeV}^{-1}$; col. (3): the error of normalization in units of $\text{cm}^{-2} \text{s}^{-1} \text{MeV}^{-1}$; col. (4): the photon index; col. (5): the error of the photon index; col. (6): the curvature index of the log-parabola function; col. (7): the error of the curvature index; col. (8): the pivot energy in units of MeV; col. (9): the same observation periods as the VHE observation. The “–” symbol indicates a null value.

^a Power-law function. The other sources are the log-parabola function.

the stronger beaming effect for those sources observed in the flaring state.

5. Discussion

Fossati et al. (1998) calculated the SEDs for 126 blazars, investigated the correlations between radio (5 GHz) luminosity and synchrotron peak luminosity and between γ -ray luminosity and synchrotron peak frequency, and consequently proposed the “blazar sequence.” This sequence was later confirmed with a larger sample of Fermi sources (Ghisellini et al. 2017).

The synchrotron radiation of blazars is produced by relativistic electrons moving in the magnetic field. The γ -ray emission is attributed to the inverse Compton process, but different seed photons supply FSRQs and BL Lacs. FSRQs are considered to contain a soft-photon-rich environment, the soft photons of which could come from the accretion disk, the broad emission line region, or the dusty torus (Ghisellini et al. 1998; Prandini & Ghisellini 2022). Hence, the electron cooling for FSRQs is more efficient than that for BL Lacs and the energy of relativistic electrons in BL Lac jets is more likely powerful than those in FSRQ jets. As a result, the energy of soft photons produced through synchrotron radiation in BL Lac jets is higher than that in FSRQ jets, leading to BL Lacs having a higher synchrotron peak frequency (Ghisellini et al. 1998). These seed photons could be scattered into an extremely high energy range, for example the TeV range, mainly by the population of relativistic electrons through the synchrotron self-Compton (SSC) process for BL Lacs and through the external Compton process for FSRQs. The more dramatic electron cooling efficiency creates the lower energy of relativistic electrons and the subsequent lower synchrotron peak frequency. However, BL Lacs have a less efficient electron cooling process in which the relativistic electrons can preserve energy and result in a higher energy of the synchrotron peak and the production of SSC TeV emission.

In this work, we expand the study of the “blazar sequence” to the TeV band. We notice that there is an anticorrelation between the observed TeV luminosity and the observed

synchrotron peak frequency during the flaring state, and there is no significant anticorrelation between the observed TeV luminosity and the observed synchrotron peak frequency for the sources in the quiescent state, as seen in Figure 1. In the top panel of Figure 1, we consider and analyze the correlation for FSRQs, BL Lacs, and BCUs together as a whole sample, because we have an extremely limited sample size of FSRQs and BCUs. Further, the empty circled region, with a synchrotron peak frequency ranging from 10^{14} up to 10^{16} , in this panel is intriguing. Those sources located in this region should be mostly considered as ISPs, with intermediate TeV luminosity compared to TeV J0222+430 (3C 66A) and those sources below the circle. These sources, somehow, in this region are not detected. Therefore, the anticorrelation is diluted in the quiescent state. In this case, our results indicate a trend for the blazar sequence in the TeV band in the quiescent state of blazars, which is plotted as a dashed line in the top panel of Figure 1. However, one should bear in mind that it is possible that there are no more other sources in this empty circle, because these potential sources are detectable to TeV telescopes. In this case, the anticorrelation trend for the quiescent state does not exist, and the TeV blazar sequence appears only in the flaring state. To sum up, the existence of the TeV blazar sequence in the quiescent state is uncertain.

Fan et al. (2017) studied the blazar sequence in the radio, optical, X-ray, and γ -ray bands using a sample of 86 flaring blazars. They noticed that the blazar sequence exists in the diagram of observed quantities and the sequence disappears when the intrinsic quantities are considered, suggesting that the blazar sequence is a consequence of the beaming effect. Yang et al. (2022b), an extended work of Fan et al. (2017) with a larger sample, also found the blazar sequence exists for the observed quantities and disappears for the intrinsic quantities. Our results in Figure 2 are consistent with the conclusion of Fan et al. (2017) and Yang et al. (2022b). In the top panel of Figure 2, we notice that there are two FSRQs mixed with the BL Lacs. We reanalyzed the correlation after removing the two FSRQs; the linear regressions are plotted in the top panel of

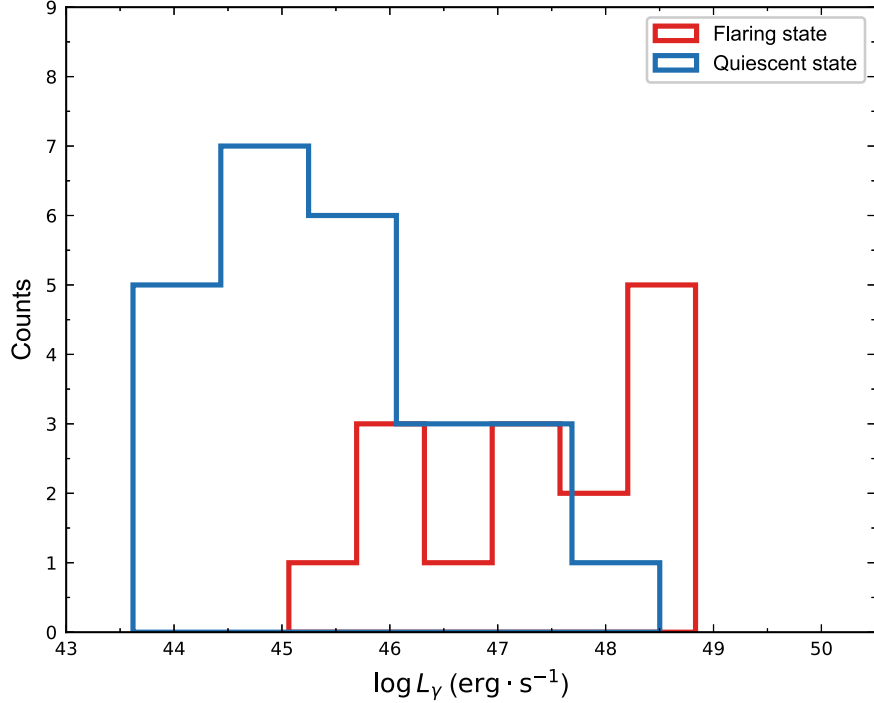


Figure 3. Distribution of Fermi γ -ray luminosity in both quiescent state and flaring state. The blue histogram denotes the quiescent state and the red histogram denotes the flaring state.

Figure 2 with dotted lines and give the formulas

$$\log L_{1\text{ TeV}}^{\text{in}} = (1.45 \pm 0.20) \log \nu_p^{\text{in}} + (17.90 \pm 3.03), \quad (14)$$

with $r = 0.77$ and $p < 10^{-4}$ for the case of $q = 2 + \alpha$, and

$$\log L_{1\text{ TeV}}^{\text{in}} = (1.78 \pm 0.22) \log \nu_p^{\text{in}} + (11.86 \pm 3.38), \quad (15)$$

with $r = 0.80$ and $p < 10^{-4}$ for the case of $q = 3 + \alpha$. For the lower panel of Figure 2, we notice TeV 1159+292 (Ton 599), shows an extremely powerful TeV emission, apart from the flaring sample population, which is linearly distributed along the regression line. Ton 599 was occurring in an extraordinary γ -ray flaring state. This flare was detected by AGILE (the Astro-rivelatore Gamma a Immagini Leggero) from 2017 December 16–18 (MJD 58103.24–58105.24; Bulgarelli et al. 2017) and VERITAS from 2017 December 15–16 (MJD 58102–58104; Mukherjee 2017). The average flux on the two nights was $F(E \geq 100 \text{ GeV}) = (1.0 \pm 0.1) \times 10^{-10} \text{ ph cm}^{-2} \text{ s}^{-1}$, or 16% of the Crab Nebula flux above the same threshold (Mukherjee 2017). According to our fitting results for the VHE spectrum, we find the photon spectral index of Ton 599 is $\Gamma = 0.16$ (see Figure 5) and the spectrum is so hard that it has an extremely high luminosity in TeV emission.

We thus reanalyze the linear regression without Ton 599, the results of which are plotted in the lower panel of Figure 2 as dotted lines and expressed as

$$\log L_{1\text{ TeV}}^{\text{in}} = (1.11 \pm 0.26) \log \nu_p^{\text{in}} + (24.51 \pm 3.65), \quad (16)$$

with $r = 0.73$ and $p = 5.80 \times 10^{-4}$ for the case of $q = 2 + \alpha$, and

$$\log L_{1\text{ TeV}}^{\text{in}} = (1.37 \pm 0.29) \log \nu_p^{\text{in}} + (19.87 \pm 4.15), \quad (17)$$

with $r = 0.76$ and $p = 2.65 \times 10^{-4}$ for the case of $q = 3 + \alpha$.

It is clear that the correlations become more significant when we remove these particular sources. In addition, our results shown in Figure 2 indicate that the TeV blazar sequence is caused by the beaming effect, which is consistent with the results in Fan et al. (2017) and Yang et al. (2022b). Moreover, we find these TeV sources have larger average Fermi GeV γ -ray luminosity during the TeV flaring state than during the quiescent state, as shown in Figure 3. These results suggest blazars in a flaring state show a stronger beaming effect and display a more significant blazar sequence than those blazars in a quiescent state.

6. Conclusions

In this work, for the purpose of studying the so-called “blazar sequence” in the TeV energy range, we collected a sample of 48 TeV blazars in the quiescent state and 21 TeV blazars in the flaring state with available VHE spectrum information, synchrotron peak frequency, and Doppler factor from the literature. We investigated the correlations between the observed/intrinsic TeV luminosity and the observed/intrinsic synchrotron peak frequency, which is representative of the blazar sequence.

Our main conclusions are as follows:

1. There is no correlation between TeV luminosity and synchrotron peak frequency for the observed values in the quiescent state; however, there is a strong anticorrelation between these two parameters in the flaring state. Therefore, we suggest that the TeV blazar sequence is present in the flaring state.
2. The correlation for the intrinsic values shows a strong positive correlation in both the quiescent state and flaring state. This result demonstrates that the blazar sequence is not present for the intrinsic values and the anticorrelation

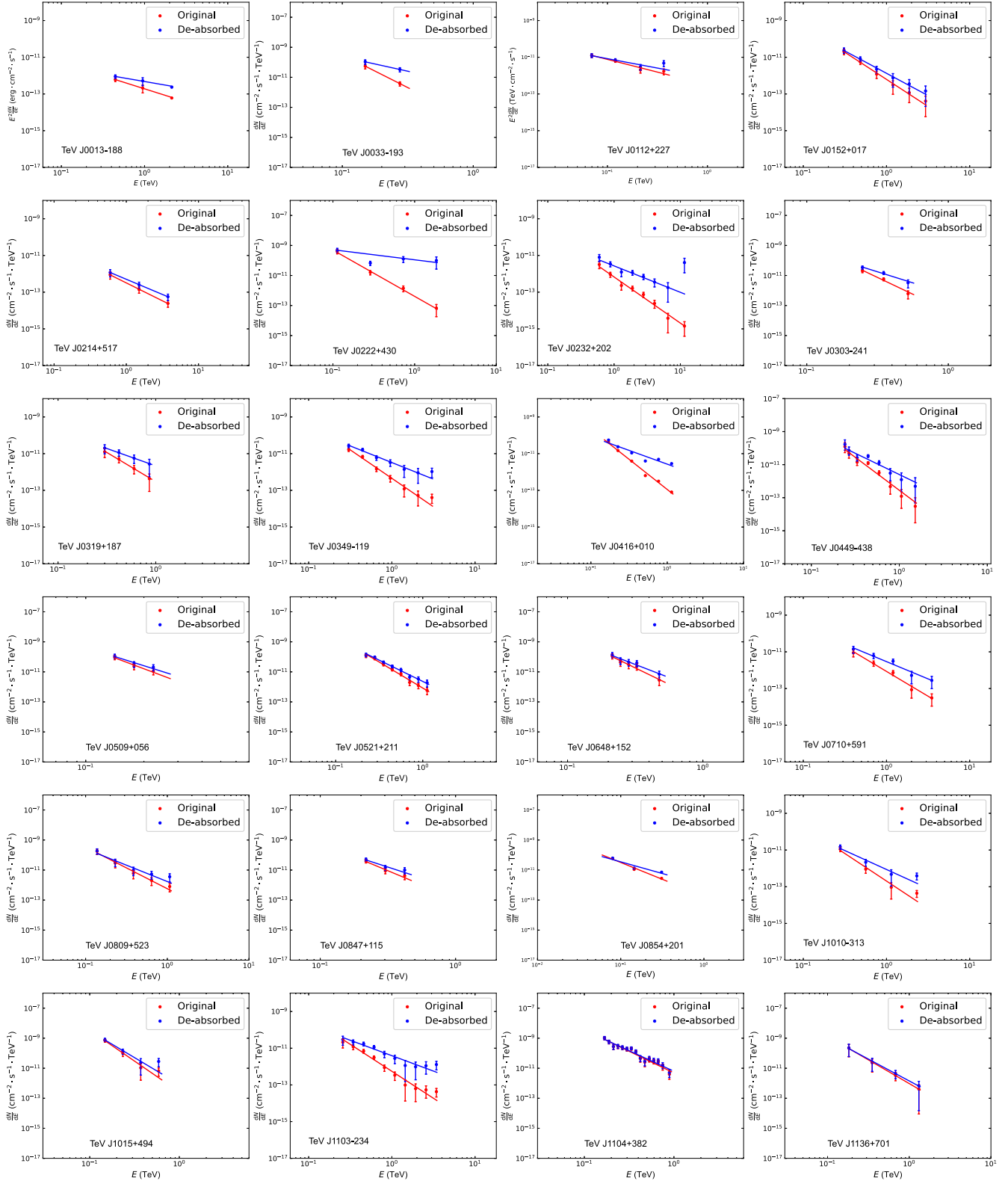
- for the observed quantities derives from the beaming effect.
3. Through a comparison of Fermi γ -ray luminosity between the quiescent state and flaring state, we find that the Fermi γ -ray luminosity of the flaring state is greater than that of the quiescent state, which means the Doppler factor in the flaring state is greater than that in the quiescent state. We suggest the presence of the blazar sequence or the anticorrelation between TeV luminosity and synchrotron peak frequency may be due to the stronger beaming effect in the flaring state.

We thank the support of the Key Laboratory for Astrophysics of Shanghai. H.B.X. acknowledges the support from the National Natural Science Foundation of China (grant No. NSFC 12203034) and from the Shanghai Science and Technology Fund (grant No. 22YF1431500); J.H.F. acknowledges the support from the NSFC (grant Nos. NSFC

U2031201, NSFC 11733001, and U2031112), Scientific and Technological Cooperation Projects (2020–2023) between the People’s Republic of China and the Republic of Bulgaria, Guangdong Major Project of Basic and Applied Basic Research (grant No. 2019B030302001), a science research grant from the China Manned Space Project with grant No. CMS-CSST-2021-A06, and support from the Astrophysics Key Subjects of Guangdong Province and Guangzhou City. This research was partially supported by the Bulgarian National Science Fund of the Ministry of Education and Science under grant Nos. KP-06-H28/3 (2018), KP-06-H38/4 (2019), KP-06-KITAJ/2 (2020), and KP-06-PN68/1(2022).

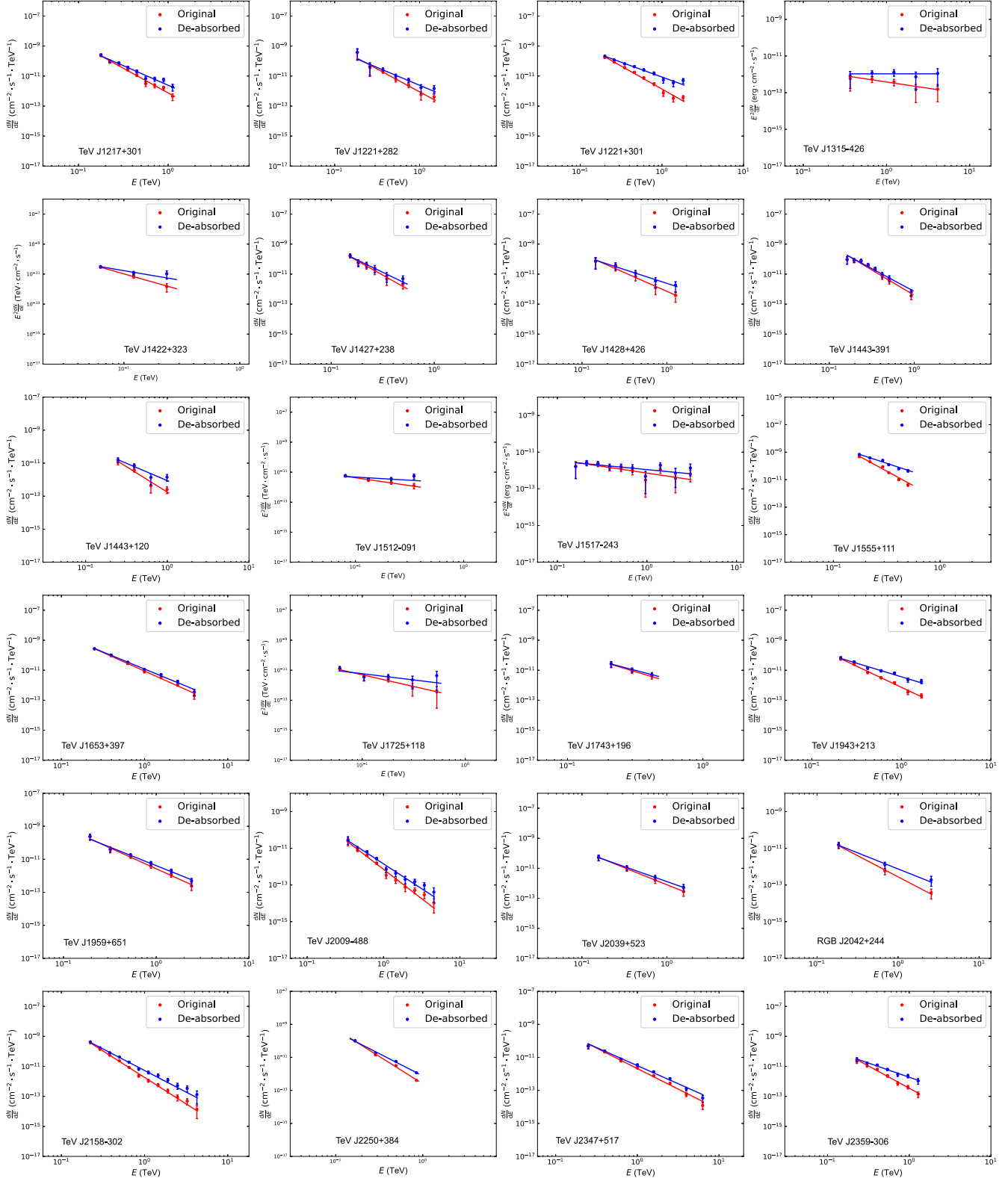
Appendix Fitting Results of the Very-high-energy Spectrum

In Figures 4 and 5, we show the original spectrum and the deabsorbed spectrum fitting results for the quiescent state and the flaring state.



(a)

Figure 4. The fitting results of the VHE spectrum of the quiescent state for each source. The red circles denote the original spectrum and the blue ones denote the deabsorbed spectrum corrected by the EBL model from Franceschini et al. (2008).



(b)

Figure 4. (Continued.)

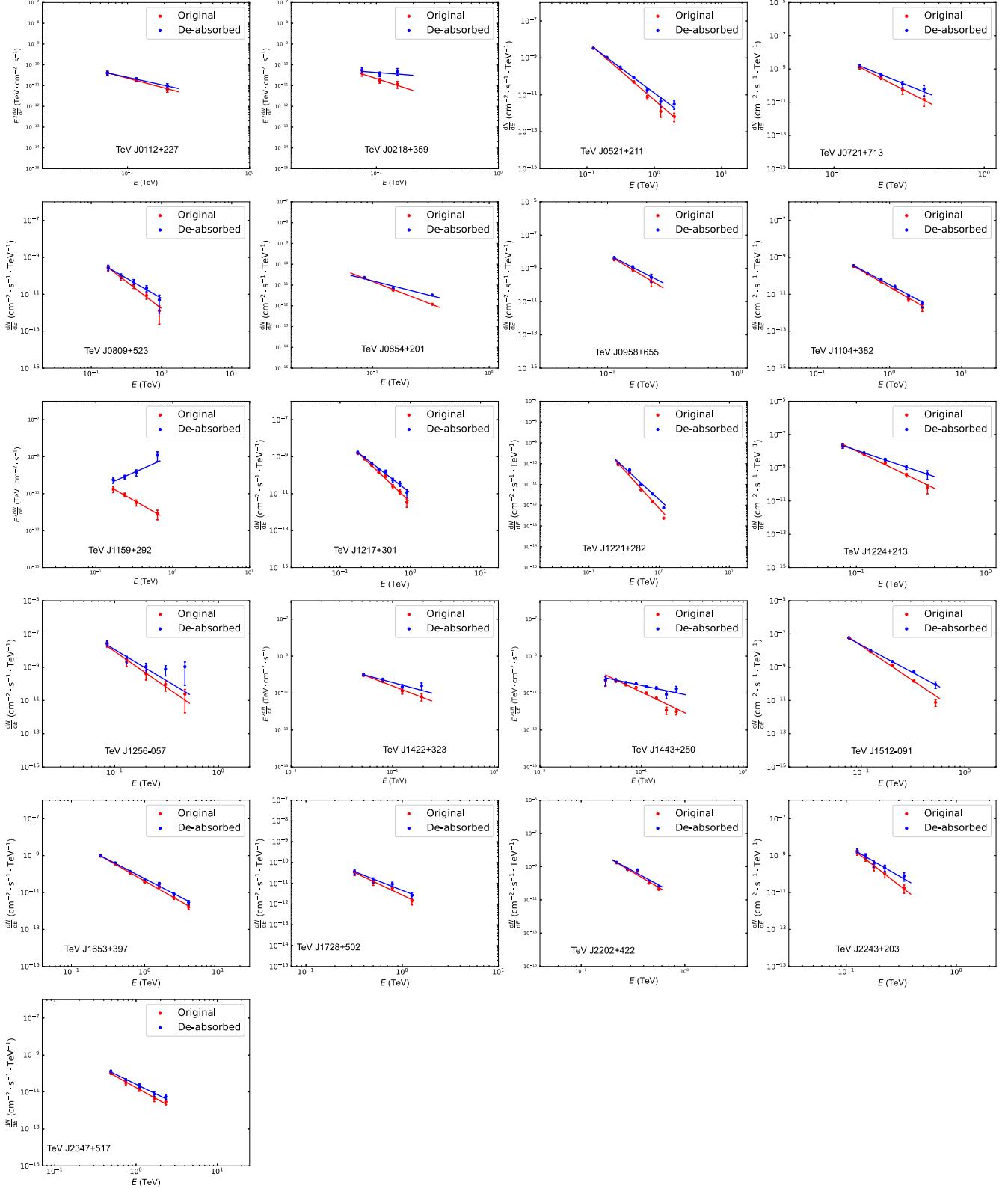


Figure 5. The fitting results of the VHE spectrum of the flaring state for each source. The red circles denote the original spectrum and the blue ones denote the deabsorbed spectrum corrected by the EBL model from Franceschini et al. (2008).

ORCID iDs

- Hubing Xiao <https://orcid.org/0000-0001-8244-1229>
 Junhui Fan <https://orcid.org/0000-0002-5929-0968>
 Rumen S. Bachev <https://orcid.org/0000-0002-0766-864X>
 Xiangtao Zeng <https://orcid.org/0000-0002-0551-5615>
 Rui Xue <https://orcid.org/0000-0003-1721-151X>

References

- Abdalla, H., Adam, R., Aharonian, F., et al. 2020, *MNRAS*, **494**, 5590
 Abdo, A. A., Ackermann, M., Agudo, I., et al. 2010, *ApJ*, **716**, 30
 Abdollahi, S., Acero, F., Baldini, L., et al. 2022, *ApJS*, **260**, 53
 Abeysekara, A. U., Archambault, S., Archer, A., et al. 2016, *MNRAS*, **459**, 2550
 Abeysekara, A. U., Archambault, S., Archer, A., et al. 2017, *ApJS*, **233**, 7
 Abeysekara, A. U., Archer, A., Benbow, W., et al. 2018, *ApJL*, **861**, L20
 Acciari, V. A., Aliu, E., Arlen, T., et al. 2009a, *ApJ*, **695**, 1370
 Acciari, V. A., Aliu, E., Arlen, T., et al. 2010a, *ApJL*, **715**, L49
 Acciari, V. A., Aliu, E., Arlen, T., et al. 2010c, *ApJL*, **708**, L100
 Acciari, V. A., Aliu, E., Arlen, T., et al. 2011, *ApJ*, **738**, 169
 Acciari, V. A., Aliu, E., Aune, T., et al. 2009b, *ApJ*, **703**, 169
 Acciari, V. A., Aliu, E., Beilicke, M., et al. 2008, *ApJL*, **684**, L73
 Acciari, V. A., Aliu, E., Beilicke, M., et al. 2010b, *ApJL*, **709**, L163
 Acciari, V. A., Ansoldi, S., Antonelli, L. A., et al. 2020, *ApJS*, **247**, 16
 Adams, C. B., Batista, P., Benbow, W., et al. 2022a, *ApJ*, **932**, 129
 Adams, C. B., Batshoun, J., Benbow, W., et al. 2022b, *ApJ*, **924**, 95
 Aharonian, F., Akhperjanian, A. G., Barres de Almeida, U., et al. 2007a, *A&A*, **475**, L9
 Aharonian, F., Akhperjanian, A. G., Barres de Almeida, U., et al. 2007b, *A&A*, **473**, L25
 Aharonian, F., Akhperjanian, A. G., Barres de Almeida, U., et al. 2008, *A&A*, **481**, L103
 Aharonian, F., Akhperjanian, A. G., Bazer-Bachi, A. R., et al. 2007c, *A&A*, **470**, 475
 Ahnen, M. L., Ansoldi, S., Antonelli, L. A., et al. 2015, *ApJL*, **815**, L23
 Ahnen, M. L., Ansoldi, S., Antonelli, L. A., et al. 2016a, *MNRAS*, **459**, 3271
 Ahnen, M. L., Ansoldi, S., Antonelli, L. A., et al. 2016b, *A&A*, **595**, A98
 Ahnen, M. L., Ansoldi, S., Antonelli, L. A., et al. 2017, *A&A*, **603**, A31
 Albert, J., Aliu, E., Anderhub, H., et al. 2006, *ApJL*, **648**, L105
 Albert, J., Aliu, E., Anderhub, H., et al. 2007, *ApJL*, **667**, L21
 Aleksić, J., Alvarez, E. A., Antonelli, L. A., et al. 2012, *A&A*, **539**, A118
 Aleksić, J., Ansoldi, S., Antonelli, L. A., et al. 2015, *MNRAS*, **451**, 739
 Aleksić, J., Antonelli, L. A., Antoranz, P., et al. 2011, *ApJL*, **730**, L8
 Aliu, E., Anderhub, H., Antonelli, L. A., et al. 2009, *ApJL*, **692**, L29
 Aliu, E., Archer, A., Aune, T., et al. 2012, *ApJ*, **750**, 94
 Aliu, E., Archer, A., Aune, T., et al. 2015, *ApJ*, **799**, 7
 Aliu, E., Aune, T., Beilicke, M., et al. 2011, *ApJ*, **742**, 127
 Allen, C., Archambault, S., Archer, A., et al. 2017, *MNRAS*, **471**, 2117
 Archambault, S., Archer, A., Barnacka, A., et al. 2016, *MNRAS*, **461**, 202
 Archambault, S., Archer, A., Beilicke, M., et al. 2015, *ApJ*, **808**, 110
 Archambault, S., Arlen, T., Aune, T., et al. 2013, *ApJ*, **776**, 69
 Archer, A., Benbow, W., Bird, R., et al. 2018, *ApJ*, **862**, 41
 Arlen, T., Aune, T., Beilicke, M., et al. 2013, *ApJ*, **762**, 92
 Atwood, W. B., Abdo, A. A., Ackermann, M., et al. 2009, *ApJ*, **697**, 1071
 Baloković, M., Paneque, D., Madejski, G., et al. 2016, *ApJ*, **819**, 156
 Blandford, R., Meier, D., & Readhead, A. 2019, *ARA&A*, **57**, 467
 Böttcher, M., Reimer, A., & Marscher, A. P. 2009, *ApJ*, **703**, 1168
 Bulgarelli, A., Parmiggiani, N., Lucarelli, F., et al. 2017, *ATel*, **11073**, 1
 Cerruti, M., Zech, A., Boisson, C., et al. 2015, *MNRAS*, **448**, 910
 Cerruti, M., Zech, A., Boisson, C., et al. 2019, *MNRAS*, **483**, L12
 Chen, L. 2018, *ApJS*, **235**, 39
 Domínguez, A., Primack, J. R., Rosario, D. J., et al. 2011, *MNRAS*, **410**, 2556
 Fan, J.-H., Bastieri, D., Yang, J.-H., et al. 2014a, *RAA*, **14**, 1135
 Fan, J. H., Bastieri, D., Yang, J. H., et al. 2014b, *JApA*, **35**, 231
 Fan, J.-H., Wang, Y.-J., Yang, J.-H., & Su, C.-Y. 2004, *ChJAA*, **4**, 533
 Fan, J. H., Yang, J. H., Liu, Y., et al. 2016, *ApJS*, **226**, 20
 Fan, J. H., Yang, J. H., Xiao, H. B., et al. 2017, *ApJL*, **835**, L38
 Fossati, G., Maraschi, L., Celotti, A., Comastri, A., & Ghisellini, G. 1998, *MNRAS*, **299**, 433
 Franceschini, A., Rodighiero, G., & Vaccari, M. 2008, *A&A*, **487**, 837
 Gao, S., Fedynitch, A., Winter, W., et al. 2019, *NatAs*, **3**, 88
 Ghisellini, G., Celotti, A., Fossati, G., Maraschi, L., & Comastri, A. 1998, *MNRAS*, **301**, 451
 Ghisellini, G., Righi, C., Costamante, L., & Tavecchio, F. 2017, *MNRAS*, **469**, 255
 Ghisellini, G., & Tavecchio, F. 2009, *MNRAS*, **397**, 985
 Ghisellini, G., Tavecchio, F., Maraschi, L., Celotti, A., & Sbarrato, T. 2014, *Natur*, **515**, 376
 Giommi, P., Padovani, P., Polenta, G., et al. 2012a, *MNRAS*, **420**, 2899
 Giommi, P., Polenta, G., Lähteenmäki, A., et al. 2012b, *A&A*, **541**, A160
 H. E. S. S. Collaboration, Abramowski, A., Acero, F., et al. 2013, *MNRAS*, **434**, 1889
 H. E. S. S. Collaboration, Acero, F., Aharonian, F., et al. 2010a, *A&A*, **511**, A52
 H. E. S. S. Collaboration, Acero, F., Aharonian, F., et al. 2010b, *A&A*, **520**, A83
 H. E. S. S. Collaboration, Acero, F., Aharonian, F., et al. 2010c, *A&A*, **516**, A56
 H. E. S. S. Collaboration, Acero, F., Aharonian, F., et al. 2012a, *A&A*, **538**, A103
 H. E. S. S. Collaboration, Acero, F., Aharonian, F., et al. 2012b, *A&A*, **542**, A94
 H. E. S. S. Collaboration, Acero, F., Aharonian, F., et al. 2013a, *A&A*, **554**, A72
 H. E. S. S. Collaboration, Acero, F., Aharonian, F., et al. 2013b, *A&A*, **559**, A136
 H. E. S. S. Collaboration, Acero, F., Aharonian, F., et al. 2013c, *A&A*, **552**, A118
 H. E. S. S. Collaboration, Acero, F., Aharonian, F., et al. 2015, *A&A*, **573**, A31
 H. E. S. S. Collaboration, Acero, F., Aharonian, F., et al. 2021, *A&A*, **648**, A23
 Kapanadze, B., & Gurchumelia, A. 2022, *A&A*, **668**, A75
 Lin, C., & Fan, J.-H. 2016, *RAA*, **16**, 103
 Lind, K. R., & Blandford, R. D. 1985, *ApJ*, **295**, 358
 Lyutikov, M., & Kravchenko, E. V. 2017, *MNRAS*, **467**, 3876
 MAGIC Collaboration, Ansoldi, S., Antonelli, L. A., et al. 2018a, *MNRAS*, **480**, 879
 MAGIC Collaboration, Acciari, V. A., Ansoldi, S., et al. 2018b, *A&A*, **619**, A159
 MAGIC Collaboration, Acciari, V. A., Ansoldi, S., et al. 2018c, *A&A*, **619**, A45
 MAGIC Collaboration, Acciari, V. A., Ansoldi, S., et al. 2018d, *A&A*, **617**, A30
 MAGIC Collaboration, Acciari, V. A., Ansoldi, S., et al. 2021, *A&A*, **647**, A163
 MAGIC Collaboration, Albert, J., Aliu, E., et al. 2008, *Sci*, **320**, 1752
 Mao, P., Urry, C. M., Massaro, F., et al. 2016, *ApJS*, **224**, 26
 Massaro, F., Paggi, A., Errando, M., et al. 2013, *ApJS*, **207**, 16
 Mücke, A., Protheroe, R. J., Engel, R., Rachen, J. P., & Stanev, T. 2003, *APh*, **18**, 593
 Mukherjee, R., & VERITAS Collaboration 2017, *ATel*, **11075**, 1
 Nieppola, E., Tornikoski, M., & Valtaoja, E. 2006, *A&A*, **445**, 441
 Nieppola, E., Valtaoja, E., Tornikoski, M., Hovatta, T., & Kotiranta, M. 2008, *A&A*, **488**, 867
 Ouyang, Z., Xiao, H., Zheng, Y., Xu, P., & Fan, J. 2021, *Ap&SS*, **366**, 12
 Paiano, S., Landoni, M., Falomo, R., et al. 2017, *ApJ*, **837**, 144
 Potter, W. J., & Cotter, G. 2015, *MNRAS*, **453**, 4070
 Prandini, E., & Ghisellini, G. 2022, *Galax*, **10**, 35
 Scarpa, R., & Falomo, R. 1997, *A&A*, **325**, 109
 Seta, H., Isobe, N., Tashiro, M. S., et al. 2009, *PASJ*, **61**, 1011
 Stickel, M., Padovani, P., Urry, C. M., Fried, J. W., & Kuehr, H. 1991, *ApJ*, **374**, 431
 Tagliaferri, G., Foschini, L., Ghisellini, G., et al. 2008, *ApJ*, **679**, 1029
 Tavecchio, F., Maraschi, L., & Ghisellini, G. 1998, *ApJ*, **509**, 608
 Tan, C., Xue, R., Du, L., et al. 2020, *ApJS*, **248**, 27
 Urry, C. M., & Padovani, P. 1995, *PASP*, **107**, 803
 Valverde, J., Horan, D., Bernard, D., et al. 2020, *ApJ*, **891**, 170
 Xiao, H., Ouyang, Z., Zhang, L., et al. 2022, *ApJ*, **925**, 40
 Yang, J. H., Fan, J. H., Liu, Y., et al. 2022a, *ApJS*, **262**, 18
 Xue, R., Wang, Z., & Li, W. 2022, *PhRvD*, **106**, 103021
 Yang, W. X., Wang, H. G., Liu, Y., et al. 2022b, *ApJ*, **925**, 120
 Zhang, L., Chen, S., Xiao, H., Cai, J., & Fan, J. 2020, *ApJ*, **897**, 10